Energy & Environmental Science

Dynamic Article Links

Cite this: *Energy Environ. Sci.*, 2011, **4**, 4211

www.rsc.org/ees

PAPER

Self-doped $SrTiO_{3-\delta}$ photocatalyst with enhanced activity for artificial photosynthesis under visible light†

Kui Xie,[ab] Naoto Umezawa,[ac] Ning Zhang,[a] Pakpoom Reunchan,[a] Yuanjian Zhang[ab] and Jinhua Ye*[ab]

Received 2nd May 2011, Accepted 21st July 2011
DOI: 10.1039/c1ee01594j

Self-doped $SrTiO_{3-\delta}$ was prepared through a carbon-free one-step combustion method followed by a series of heat treatments in Ar at temperatures ranging from 1200 to 1400 °C. X-Ray Photoelectron Spectroscopy (XPS), Electron Paramagnetic Resonance (EPR) and High-Resolution TEM confirm the presence of Ti^{3+} in samples with oxygen vacancy accommodated in perovskite by forming Ruddlesden–Popper crystallographic shears. The UV-vis spectra and electronic structure calculations show that the oxygen vacancy and Ti^{3+} together induce an in-gap band to enhance the visible light absorption. Pulsed Adsorption of CO_2 and Temperature Programmed Desorption (TPD) experiments show that the higher oxygen deficiency tends to improve the chemical adsorption of CO_2 on the surface as well as in the bulk of $SrTiO_{3-\delta}$, especially the accommodation of CO_2 molecule in the oxygen vacancy. It is the synergetic effect of visible light absorption and chemical adsorption of CO_2 that improves the artificial photosynthesis to generate hydrocarbon fuels from CO_2/H_2O under visible light irradiation. We also demonstrated that the incorporation of oxygen from CO_2/H_2O into the oxygen vacancy of $SrTiO_{3-\delta}$ leads to the absence of oxygen evolution which therefore results in the oxidation of $SrTiO_{3-\delta}$ ($Ti^{3+} \rightarrow Ti^{4+}$).

Introduction

There is growing evidence for, and acceptance of, the role of the rising level of anthropogenic emissions of greenhouse gas CO_2 into the atmosphere in contributing to potentially dangerous climate change.[1] This is mainly the result of our heavy reliance on finite fossil resources that also leads to potential energy crisis. Significant efforts are being devoted to solar cells,[2] solid oxide electrolysis cells,[3,4] solid oxide fuel cells[5] as well as solar fuel conversion,[6–9] to carry the renewable energy from where it is available to its point of use. At present, hydrogen has been widely considered as the only renewable energy carrier that can be synthesized efficiently; however, some technical barriers related to its storage and distribution have contributed to the resistance that hydrogen has encountered in becoming practically viable despite a high energy density and zero carbon emission. Synthetic hydrocarbon fuels have therefore been proposed as an alternative form of energy carrier taking into account that they would be compatible with the existing energy infrastructures in addition to

[a]*Photocatalytic Materials Center, National Institute for Materials Science, Tsukuba, Ibaraki, 3050047, Japan. E-mail: Jinhua.YE@nims.go.jp*
[b]*International Center for Materials Nanoarchitectonics, National Institute for Materials Science, Tsukuba, Ibaraki, 3050047, Japan*
[c]*PRESTO, Japan Science and Technology Agency (JST), 4-1-8 Honcho Kawaguchi, Saitama, 332-0012, Japan*

† Electronic supplementary information (ESI) available: More information on experimental and discussions, ICP element analysis, EPR, XPS, BET, TPD, and TEM. See DOI: 10.1039/c1ee01594j

Broader context

Growing concerns over the consequences of global climate change are forcing a major shift in the energy portfolio from the current dominance of fossil fuels towards a rich and diverse mix of energy supply based upon renewable and environmentally benign sources. Emerging technologies such as solar fuel conversion and solar photovoltaics represent recent technical breakthroughs in harnessing renewable solar energy. The progressive move to the clean energy carrier, hydrogen, is seriously impeded by the economic challenge of the unbalanced costs in all aspects of hydrogen production, storage and distribution. In the short and medium terms, synthetic hydrocarbon fuels appear to be the ideal energy carriers for adapting the world to a sustainable energy cycle. Direct visible-light artificial photosynthesis on semiconductor photocatalyst to generate methane, the major component of natural gas, through a photochemical reduction of carbon dioxide in the presence of water is demonstrated in the present work. This new strategy in producing synthetic hydrocarbon fuels can deliver a carbon neutral renewable energy cycle.

their inherent advantages, such as high H/C ratio and the flexibility in hydrocarbon-based power.[10] Through mimicking the natural photosynthesis, some useful hydrocarbons could be directly produced from CO_2/H_2O in an artificial photosynthesis process based on semiconductor photocatalyst powders. The recycling of CO_2 would advance us into a carbon-neutral renewable energy cycle. In this process, a semiconductor photocatalyst acts as a microelectrochemical cell which is activated by solar energy. The photo-excited electrons initiate the electrochemical reduction of H_2O into a hydrogen species that simultaneously reduces CO_2 into useful hydrocarbons.[11,12]

Perovskite-type oxide $SrTiO_3$ has been well known as a wide-gap semiconductor photocatalyst in the field of solar hydrogen.[13,14] Pure $SrTiO_3$, however, is not a good photocatalyst candidate, because it is only active under ultraviolet (UV) irradiation. Many studies have tried to introduce various dopants, such as Fe, C, N and Cr, to extend the light absorption to the visible region.[15–18] In contrast, the self-doping of oxygen vacancy is of essence since the oxygen vacancy is the fundamental and intrinsic defect in perovskite oxide and hence gives the critical impacts on their optical properties. In addition, the higher oxygen deficiency tends to bring on linear vacancy ordering with defect–defect interaction in the perovskite and therefore induces a new in-gap band that might enhance visible light absorption according to some theoretical calculations.[19,20] On the other hand, it is believed that reduced $SrTiO_3$ has the ability to chemically adsorb and activate CO_2, especially to incorporate molecular CO_2 in the oxygen vacancy in the form of carbonate ion to act as active site for heterogeneous CO_2 reduction;[21,22] however, to the best of our knowledge, improvement of chemical absorption of CO_2 has not been reported to facilitate the photoreduction of CO_2 on semiconductor photocatalysts.

In this work, we report self-doped $SrTiO_{3-\delta}$ photocatalysts with enhanced visible light activity for artificial photosynthesis from CO_2/H_2O to produce useful hydrocarbon fuels. The oxygen deficiency of $SrTiO_{3-\delta}$ photocatalysts was continuously tuned to improve the visible light absorption as well as the chemical adsorption of CO_2. A systematic theoretical calculation was also performed to understand the electronic structure and the origin of visible light absorption of $SrTiO_{3-\delta}$ photocatalyst. After that, the artificial photosynthesis with CO_2/H_2O was evaluated under visible light and the oxidized species was also identified when reduced product was produced.

Experimental

The self-doped $SrTiO_{3-\delta}$ powders were first prepared by a carbon-free combustion method from TiN and $Sr(NO_3)_2$ in air.[23] In this process, 0.05 mol TiN and 0.05 mol $Sr(NO_3)_2$ were dissolved in 30% H_2O_2 (pH $\approx$ 1) and heated at 90 °C under magnetic stirring. Finally, the obtained green powders were fired at 1200 °C for 20 h in air to get the final yellow powder sample. In this process H_2O is used to oxidize the majority of Ti^{3+} into Ti^{4+}, whereas the Ti^{3+} residual in the precursors is used to introduce oxygen deficiency in $SrTiO_{3-\delta}$. XRD for phase detection was performed with a RIGAKU Rint-2000 X-ray diffractometer equipped with graphite monochromatized Cu-K_α radiation (0.5° per min, $\lambda = 1.54178$ Å). XRD data for Rietveld refinement were recorded on a Stoe Stadi-P diffractometer with Cu $K_{\alpha 1}$ radiation (Stoe & CieGmbH, Germany) and analyzed using GSAS software. The N residual was analyzed with an ICP Mass Spectrometer LECO Co. TC-436AR and Pulsed furnace-Infrared rays detector with Si_3N_4 (JCRM, R003, $N = 39.0\%$) as the standard reference heated at 110 °C for 120 min. The Electron Paramagnetic Resonance (EPR) of the samples was recorded at 120 K to confirm the presence of high spin Ti^{3+} as well as oxygen deficiency on a JES-FA200 Electron Spin Resonance Spectrometer. X-Ray Photoelectron Spectroscopy (XPS) was performed on a Thermo ESCALAB 250 using monochromatized Al K_α at $h\nu = 1486.6$ eV to analyze the surface of the sample powder. The binding energies were calibrated to the C_{1s} peak at 284.6 eV. To further investigate the stability of oxygen deficient $SrTiO_{3-\delta}$, the yellow sample powder was treated in pure oxygen at 1200 °C for 48 h and illuminated under UV + vis irradiation for 360 h, respectively. After that, the crystal structure and optical properties were examined in an ambient environment.

To induce more oxygen deficiency and Ti^{3+} in $SrTiO_{3-\delta}$, the powders prepared in air were divided into 5 batches and treated in Ar at 1200, 1250, 1300, 1350 and 1400 °C, for 20 hours, respectively. XRD, EPR and XPS (under the same conditions) were also performed to further characterize the samples after treatments. Scanning Electron Microscopy (SEM) images were recorded to observe the morphology with scanning electron microscope (JEOL 6700F field emission scanning electron microscope). Brunauer–Emmett–Teller (BET) measurements were carried out to analyze the surface areas on a BELSORP II Surface Area Analyzer. Transmission Electron Microscopy (TEM) was performed to observe the defects in the bulk of a 1400 °C sample with a JEOL 2100F field emission transmission electron microscope operated at 200 kV. UV-visible diffuse reflectance spectra of the powder samples were recorded with a Shimadzu UV-2500 Spectrophotometer at room temperature in air. The Pulsed Adsorption of CO_2 and Temperature Programmed Desorption (TPD) of CO_2 were recorded with a Micromeritics 2000. Here the powder samples were pre-treated in air at 400 °C for 1 h to eliminate absorbed species and then treated at 200 °C in Ar for 1 h before Pulsed Adsorption of CO_2. The Temperature Programmed Desorption of CO_2 was tested from room temperature to 800 °C at 10 °C min^{-1} with He gas carrier. The details of measurement parameters and program are shown in the ESI†.

To confirm the C element in hydrocarbon products indeed from the photoreduction of CO_2 in the presence of H_2O, a series of control experiments were carefully conducted with different gas precursors, such as Ar, CO_2, H_2O, and H_2O/CO_2, under visible light irradiation or in the dark. In this process, 1200 °C $SrTiO_{3-\delta}$ photocatalyst powder (0.3 g) loaded with 0.3% Pt cocatalyst (weight ratio) was utilized for the control experiments. All the experiments were carried out for 3 h and the sampling was carried out one time per hour. The light source was a 300 W Xe lamp equipped with a 420 nm filter (*ca.* 53.1 mW cm^{-2}). In the first control experiment under irradiation, the gas precursor was only pure Ar to check the gas leakage and adsorbed organic chemicals. In this experiment, no gas leakage and adsorbed organic were detected. In the second control experiment, only pure CO_2 was utilized for photo-reduction under irradiation; however, no CO and O_2 were detected, indicating that CO_2 cannot be directly photo-split. In the third control experiment

under irradiation, 2% H_2O + 98% Ar were utilized as gas precursors; however, no hydrogen was detected which shows the gaseous H_2O cannot be directly split under irradiation. In the fourth experiment, 2% H_2O + 98% CO_2 were utilized as gas precursors but the experiment was carried out under dark. Here no organic chemical, hydrogen and CO were detected because artificial photosynthesis was not achieved under dark. On the other hand, all these results also demonstrate the absence of carbon residual because any carbon residual would lead to the generation of H_2 or CO. Actually, any carbon residual was removed after the treatment of the sample at 1200 °C in air for 20 h.

After that, the 5 photocatalysts (0.3 g) loaded with 0.3% Pt (weight ratio) were utilized for the artificial photosynthesis with 2% H_2O + 98% CO_2 under visible irradiation. The product was analyzed with Gas Chromatography. (The organic chemicals were analyzed using a GC GC-14B, Shimadzu Corp., Japan and the oxygen was detected with a GC Shimadzu GC-8A equipped with a thermal conductor detector TCD.) To check the influence of Pt co-catalyst, the 1400 °C $SrTiO_3$ sample without Pt loading was utilized to perform artificial photosynthesis under the same conditions. The apparent quantum yield at a wavelength of 600 ± 15 nm was measured under the light intensity of 56.1 μW cm^{-2}. The apparent quantum yield was calculated according to the equation:[7] A.Q.Y. = $[N(CH_4) \times 8]/N(\text{photons}) \times 100\%$, where $N(CH_4)$ and N(photons) signify the molecular number of CH_4 generated in unit time and the number of incident photons in unit time, respectively. (One CH_4 molecule consumes 8 electrons as shown: $CO_2 + 8e^- + 8H^+ \rightarrow CH_4 + 2H_2O$.)

Electronic structure calculations

To understand the electronic structure of self-doped $SrTiO_{3-\delta}$, we performed density functional calculations based on the local density approximation (LDA) + U approach.[24,25] Projector-augmented wave pseudopotentials were employed as implemented in the VASP code.[26,27] The valence configurations of the pseudo-potentials were $4s^24p^65s^2$ for Sr, $3p^63d^34s^1$ for Ti and $2s^22p^4$ for O. The energy cutoff for the plane-wave basis set expansion was set at 500 eV. The Monkhorst–Pack k-point sets of 6 × 6 × 6 and 2 × 2 × 2 were used for a 5 atom unit cell and a 80 atom supercell of cubic $SrTiO_3$, respectively. We applied U to Ti d and O p (U(Ti d) = 9.14 eV and U(O p) = 5.32 eV) which were determined so as to reproduce the experimental band gap (3.2 eV). The importance of applying U to O p as well as Ti d states was discussed elsewhere.[28] The 5 atom unit cell was fully relaxed for atomic positions and cell volume. The optimized lattice constant (3.92 Å) is in good agreement with an experimental value (3.905 Å).[29] The 80 atom supercell was generated by extending the unit cell for 2 × 4 × 2. Four oxygen atoms were removed from the supercell to create model structures of $SrTiO_{2.75}$, which generally correspond to the composition ratio of the 1400 °C sample.

To set up a realistic model for the reduced $SrTiO_3$, we constructed four different model structures (model A–D) with different configurations of lined oxygen vacancies as shown in Fig. 1(a)–(d), respectively. In the figure, the 80 atom supercell was extended along the x and z direction twice for visualization. Sr and O atoms are not shown in the figure. These model structures are relaxed not only for atomic positions but also for the cell volume (lattice constants). We found that all the models give the same trend in terms of the change in lattice constants: a and b decrease while c increases with respect to those of the perfect crystal, in consistent with our experimental observation (Table 1). The small difference might be attributed to the overestimation of oxygen deficiency according to EPR and XRD results. The total energies of models A, B, and C are higher than that of model D by 0.15 eV, 0.01 eV, and 0.39 eV, respectively. Thus, model D was adopted for the discussions below. Fig. 2(a)–(d) show the partial charge densities corresponding to the four occupied gap states at gamma point associated with oxygen vacancies in model D. It is clearly shown that the defect levels mainly consist of the Ti d–Ti d bonding states across the vacancy sites.

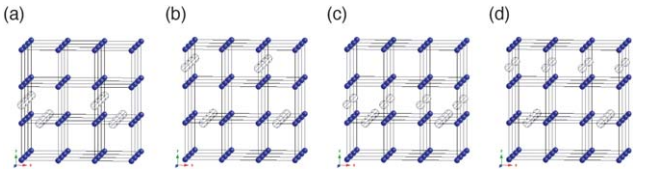

Fig. 1 Model structures for the reduced $SrTiO_3$ in which lined oxygen vacancies are placed in different configurations: (a) model A, (b) model B, (c) model C, and (d) model D. These figures are created by extending the 80 atom supercell by 2 × 1 × 2 for the visualization purpose. Blue particles and striped circles represent the positions of Ti atoms and oxygen vacancies, respectively, while Sr and O atoms are not shown in these figures.

Table 1 Lattice constants for the relaxed model structures determined by LDA + U compared to experimental values for the sample annealed at 1400 °C. The numbers in parentheses indicate the percentage of the change of the lattice constants with respect to that of pristine $SrTiO_3$ (3.92 Å) for theory and (3.905 Å) for experiment

	a/Å	b/Å	c/Å
Model A	3.89 (−0.66%)	3.88 (−0.95%)	3.95 (0.72%)
Model B	3.90 (−0.49%)	3.89 (−0.67%)	3.94 (0.42%)
Model C	3.90 (−0.56%)	3.90 (−0.56%)	3.94 (0.47%)
Model D	3.89 (−0.72%)	3.89 (−0.67%)	3.94 (0.58%)
Experiment	3.895 (−0.26%)	3.895 (−0.26%)	3.9161 (0.28%)

Results and discussions

The $SrTiO_{3-\delta}$ photocatalyst prepared at 1200 °C in air is yellow in colour showing the sample would be visible light active. As

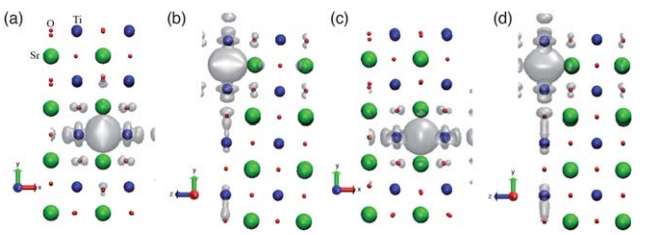

Fig. 2 Partial charge densities (gray) corresponding to the four occupied states in the band gap at gamma point for model D. Here, green, blue, and red particles denote Sr, Ti, and O atoms, respectively. The isosurface is at 0.01 electrons $Å^{-3}$.

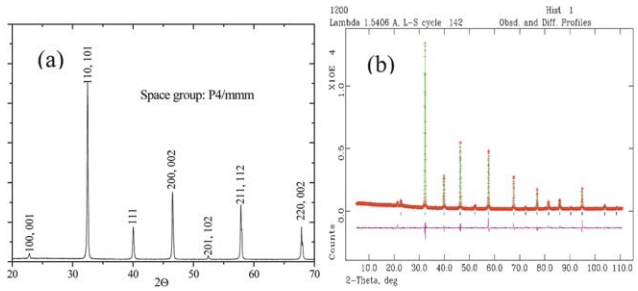

Fig. 3 (a) XRD spectra and (b) XRD Rietveld refinement (R_{wp} = 0.1104, $R_p = 0.0823$, $\chi^2 = 2.857$) of the as-prepared sample at 1200 °C in air.

shown in Fig. 3(a), the XRD of the as prepared sample only shows the strong peaks corresponding to $SrTiO_{3-\delta}$ with space group *P4/mmm*. Fig. 3(b) shows the XRD Rietveld refinement which discloses the nominal chemical formula $SrTiO_{2.91}$ as well as the oxygen deficiency $\delta = 0.09$. The yellow colour of the sample also demonstrates the high-temperature stability of the photocatalyst. In order to check if there is N element residual in the sample, ICP Mass Spectroscopy was conducted with the Si_3N_4 reference. As shown in Table S1*†, the residual of N is already beyond the detection limit of ~0.01%, which shows the complete exchange between N and O after heat treatment in air at such a high temperature. This result is also consistent with other reports where N doped solid oxide materials tend to completely release N at around 500–900 °C in air.[30] To further investigate the stability of oxygen deficient $SrTiO_{3-\delta}$, two samples were treated in pure oxygen at 1200 °C for 48 h and illuminated under UV + vis irradiation for 360 h, respectively. As shown in Fig. 4(a) and (b), the optical property and crystal structure of $SrTiO_{3-\delta}$ are remarkably stable without any change or degradation after UV + vis irradiation in air for 360 h. In addition, the $SrTiO_{3-\delta}$ is high-temperature stable. The crystal structure of $SrTiO_{3-\delta}$ is highly stable and there is no degradation of optical property, even after treatment in pure oxygen at 1200 °C for 48 h.

In order to further confirm the presence of Ti^{3+} in the sample, Electron Paramagnetic Resonance (EPR) was performed at 120 K to determine the presence of unpaired electron in the sample. As shown in Fig. 5(a), the sample shows a strong EPR signal at $g = 1.975$, which is characteristic of paramagnetic Ti^{3+} ion, confirming the presence of Ti^{3+} as well as oxygen deficiency in $SrTiO_{3-\delta}$.[31] The signal $g = 1.995$ is generated by the cavity.[32]

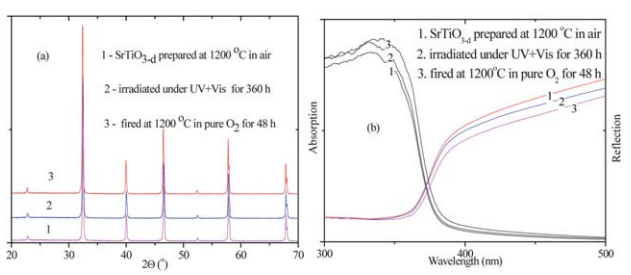

Fig. 4 XRD and UV-vis spectra of the $SrTiO_{3-\delta}$ sample (1) prepared at 1200 °C in air; (2) then illuminated under UV + vis for 360 h in air and (3) fired in pure O_2 for 48 h.

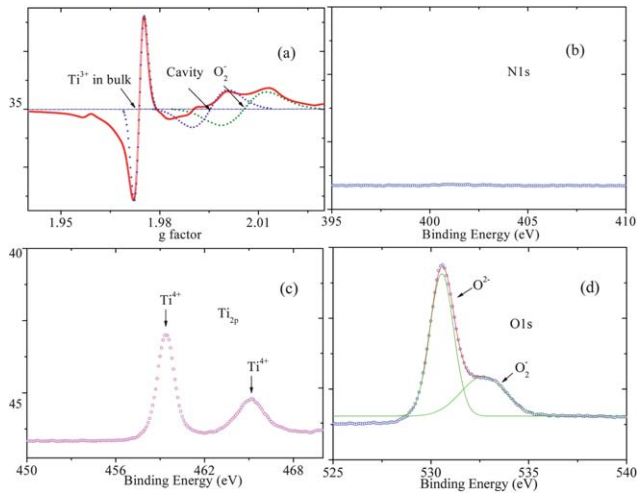

Fig. 5 EPR (at 120 K) and XPS of the 1200 °C sample prepared in air.

The signal of $g = 2.002$ is produced by the adsorption of atmospheric oxygen accommodated in the surface oxygen vacancy to generate superoxide ion O_2^-.[31,32] The adsorption of molecular oxygen is expected to lead to the oxidation of surface Ti^{3+} to Ti^{4+}, which is also confirmed by XPS results shown in Fig. 5(c), where no Ti^{3+} signal was detected. As shown in Fig. 5(d), the presence of surperoxide ion was also detected by XPS, which further confirms the adsorption of oxygen molecule in the oxygen vacancy on the photocatalyst surface. Fig. 5(b) shows the absence of the XPS signal of N_{1s} which is consistent with the result of ICP mass spectroscopy. It is reasonable to conclude that the Ti^{3+} only exists in the bulk of self-doped $SrTiO_{3-\delta}$ because surface Ti^{3+} seems to be oxidized.[33,34] The as prepared powders were then further treated at 1200, 1250, 1300, 1350 and 1400 °C in Ar for 20 hours to introduce more Ti^{3+} as well as oxygen vacancies in different samples, respectively.

After the above treatments in Ar, the 5 samples were analyzed using XRD, EPR, XPS, SEM and BET. The XRD as shown in Fig. 6(a) confirms the pure phase (*P4/mmm*) of the corresponding 5 samples after heat treatments in Ar at temperatures ranging from 1200 to 1400 °C. However, the right shift of 2Θ *versus* treatment temperature was also observed as shown in Fig. 6(b), which demonstrates the gradual decrease of cell volume with more oxygen loss at higher temperatures. As shown in Table 2, the cell volumes decrease *versus* treatment temperatures because

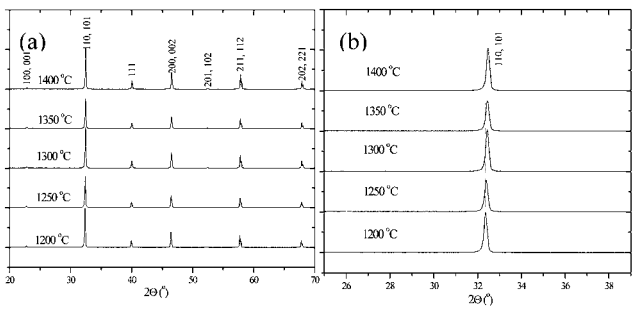

Fig. 6 (a) XRD and (b) 110 peak comparison of $SrTiO_{3-\delta}$ samples treated in Ar at different temperatures.

Table 2 Cell parameters of samples treated at different temperatures in Ar

Sample	V/Å^3	a/Å	b/Å	c/Å	α/°	β/°	γ/°	Space group
1200 °C	59.5408	3.9115	3.9115	3.8916	90	90	90	*P*4/*mmm*
1250 °C	59.5107	3.9072	3.9072	3.8982	90	90	90	*P*4/*mmm*
1300 °C	59.4877	3.8990	3.8990	3.9131	90	90	90	*P*4/*mmm*
1350 °C	59.4469	3.8970	3.8970	3.9141	90	90	90	*P*4/*mmm*
1400 °C	59.4125	3.8950	3.8950	3.9161	90	90	90	*P*4/*mmm*

the higher temperatures tend to result in more loss of oxygen in solid oxide materials in Ar atmosphere. It should be also noted that the cell parameter c is increasing *versus* oxygen deficiency; however, a and b change in a reverse trend, which may be attributed to the formation of Ruddlesden–Popper defects as the capability of $SrTiO_3$ is rather limited to accommodate oxygen defects, as reported by Irvine and his co-workers.[35] In our work, crystallographic shears were also observed as shown in TEM (Fig. S1*(a)†), which is caused by the shifting of $1/2\langle 111\rangle$, as shown in Fig. S1*(b)†. This kind of defects results in two neighboring SrO layers with a larger facet distance along the $\langle 001\rangle$ direction as reported by Zhu and her co-workers,[36] which is the reason why c increases *versus* oxygen deficiency. Furthermore, XPS and EPR (Fig. S2*–S6*†) results together demonstrate the existence of Ti^{3+} in the bulk and superoxide ion on the surface of photocatalysts. The nominal formulae are estimated to be $SrTiO_{2.90}$, $SrTiO_{2.87}$, $SrTiO_{2.83}$, $SrTiO_{2.80}$ and $SrTiO_{2.76}$ from EPR and XRD results, respectively. The specific surface areas of the 5 samples decrease from 2.4 to 1.8, 1.2, 1.1 and 0.8 $m^2\ g^{-1}$ with treatment temperature (Table S2*†), which is attributed to the particle growth at higher temperatures as confirmed by the morphology change in SEM photos as shown in Fig. 7.

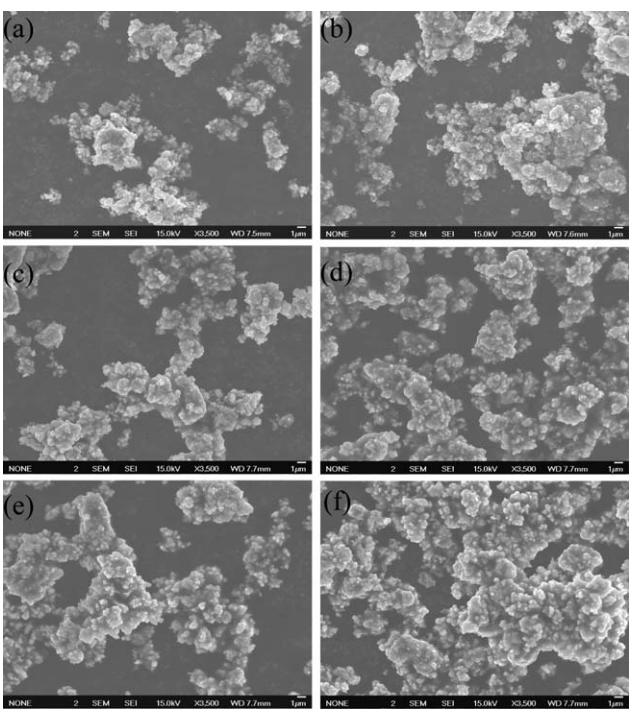

Fig. 7 SEM of $SrTiO_{3-\delta}$: (a) 1200 °C prepared in air and the samples treated in Ar at (b) 1200 (c) 1250 (d) 1300 (e)1350 and (f) 1400 °C.

Fig. 8 shows the UV-vis spectra of commercial $SrTiO_3$ and the 5 treated samples where commercial $SrTiO_3$ is only active under UV irradiation while the photoresponse of self-doped $SrTiO_{3-\delta}$ is effectively extended into the visible and near infrared region. It was also observed that the visible light absorption is positively related to oxygen deficiency. To understand the origin of the visible light absorption, we performed electronic structure calculations based on the density-functional theory (DFT) $+U$ approach.[24] To create a model structure that can reproduce the variation of the lattice constants upon oxygen reduction of $SrTiO_3$ observed in our experiments, we introduced line defects associated with oxygen vacancies along (100) and (001) directions (Fig. 9(a)) as discussed before (model D in Fig. 1). The composition ratio of our model $SrTiO_{2.75}$ nearly corresponds to that of the sample annealed in Ar at 1400 °C. The formation of such line defects in $SrTiO_{3-\delta}$ with δ larger than 0.01 was also reported elsewhere.[19,20] From the total and local density of states (DOS) for the model structure, it is understood that such a line defect creates a new band in the band gap as shown in Fig. 9(c) compared to the DOS plot for a perfect crystal (Fig. 9(b)). From the local density of states and partial charge densities corresponding to the defect-related states, we understood that the newly formed band is mainly composed of Ti d–Ti d bonding states across the vacancy sites (Fig. 2). Thus, the introduction of oxygen vacancies should promote the formation of Ti–Ti bonds, giving rise to bonding states in the band gap. Importantly, the defect-related band is occupied with electrons, and thus photoexcitations are allowed from the defect band to the conduction band within the range of visible light. We suggest that this is a possible origin of the visible light absorption enhanced in the

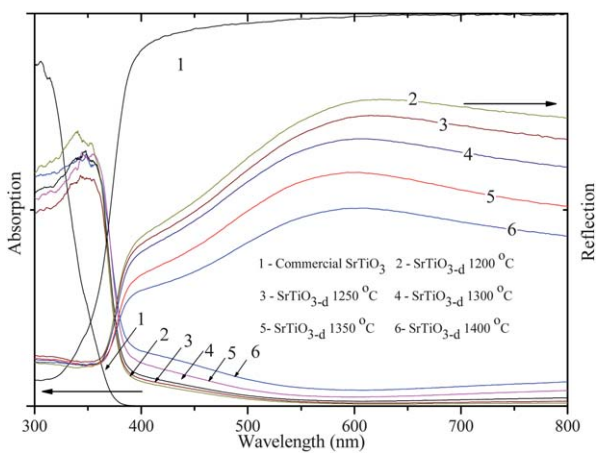

Fig. 8 UV-vis spectra of commercial $SrTiO_3$ and as prepared $SrTiO_{3-\delta}$ samples reduced in Ar at different temperatures.

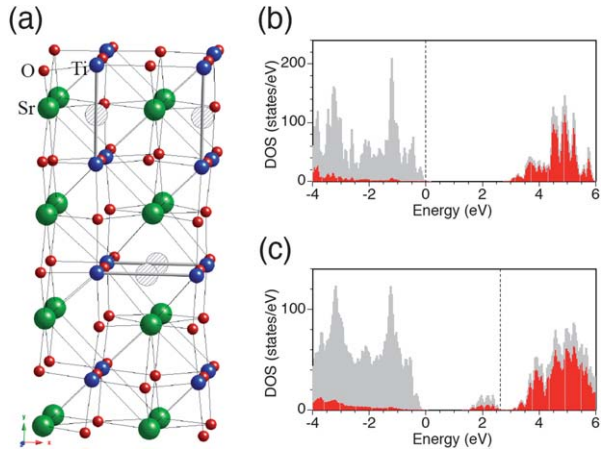

Fig. 9 (a) Relaxed geometry of the model structure used for our electronic structure calculations. Here, green, blue, and red particles denote Sr, Ti, and O atoms, respectively. The striped circles indicate the positions of oxygen vacancies. Ti–Ti bonds across the vacancy sites are shown as solid bars. The total density of states (gray) and the local density of states (red) for Ti d are also shown for (b) pristine $SrTiO_3$ and (c) the defected system. Here, the sphere of Ti radius was set to 1.323 Å. The zero energy is at the valence-band maximum of the perfect crystal of $SrTiO_3$. In Fig. 2 (c), the origin is calibrated for aligning p states of several Ti atoms located far away from the defects with respect to that of pristine $SrTiO_3$. The vertical broken line denotes the highest occupied state in each system.

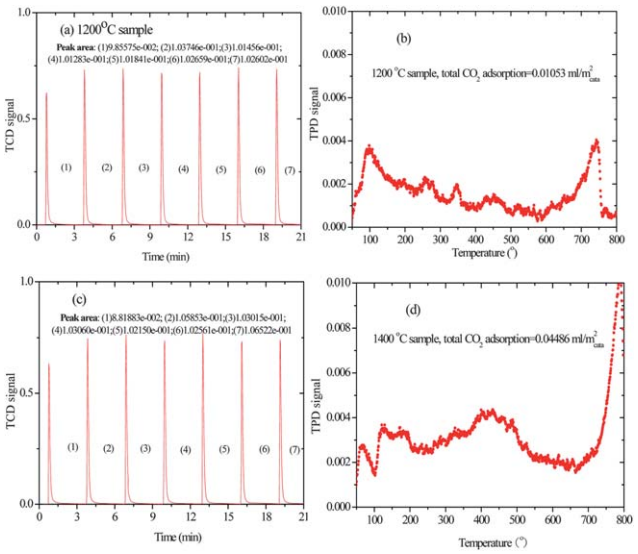

Fig. 10 Pulsed Adsorption of CO_2 (TCD signal) and Temperature Programmed Desorption (TPD signal) on 1 m^2 (surface area) 1200 °C and 1400 °C $SrTiO_{3-\delta}$ photocatalyst.

self-doped $SrTiO_{3-\delta}$. It should be also noted that the conduction band edge is not lowered upon the defect formation, which thus maintains the reduction power of photoexcited electrons.

It is popularly believed that reduced solid oxide materials have the ability to chemically adsorb and activate CO_2, especially to incorporate CO_2 molecules in the oxygen vacancy in the form of carbonate ion to act as active site for heterogeneous CO_2 reduction.[21,22] To investigate the adsorption of CO_2 on self-doped $SrTiO_{3-\delta}$ powder photocatalysts, Pulsed Adsorption of CO_2 and Temperature Programmed Desorption were performed to study the physical and chemical adsorptions of CO_2 on powder samples. Fig. 10(a) and (b) show the CO_2 adsorption and desorption on the 1200 bv°C sample, where the total adsorption of CO_2 was around 0.01 ml $m^{-2}{}_{cata}$ which was mainly dominated by physical adsorption. The chemical desorptions as shown in Fig. 10(b) at ~130 to 150 °C and ~450 °C are related to the basic sites and basic property of the $SrTiO_{3-\delta}$ surface as expected.[37,38] On the other hand, the dipole–dipole coupling between CO_2 molecules and particle surface may promote chemical adsorption that results in chemical desorption in a similar temperature region of ~130 to 150 °C.[39] It should be also noted that CO_2 desorption (TPD signal) still occurs at ~750 °C which is attributed to the release of CO_2 incorporated in the oxygen vacancy in the samples.[21,22] The Pulsed Adsorption of CO_2 and Temperature Programmed Desorption of 1250, 1300 and 1350 °C samples are shown in Fig. S7*–S9*†. As shown in Fig. 10(c) and (d), the 1400 °C sample shows ~0.04 ml $m^{-2}{}_{cata}$ where great enhancement of chemical adsorption of CO_2 was observed and the chemical adsorption dominates the total adsorption. The higher oxygen deficiency leads to enhanced chemical adsorption of CO_2, which therefore facilitates the activation of CO_2 for photosynthesis. On the other hand, the oxygen vacancy also has the ability to accommodate and chemically activate H_2O molecule for artificial photosynthesis.[40]

As shown in Table 3, a blank experiment with Ar precursor gas confirmed that there is no adventitious hydrocarbon in our system. On the other hand, there is no carbon residual in the sample because the carbon residual would lead to the evolution of CO or H_2 with CO_2 or H_2O precursor. In addition, there is no adsorption of organic chemicals on the sample as confirmed by the control experiment with H_2O/CO_2 under dark. It was also observed that only H_2O or CO_2 cannot be directly photo-split in the gaseous condition. However, the artificial photosynthesis from CO_2/H_2O was successfully achieved under visible light irradiation, which implies that CO_2 was photoreduced in the presence of H_2O. The hydrocarbons from CO_2/H_2O might be related to the electrochemical reaction of hydrogen species with activated carbon dioxide on self-doped $SrTiO_{3-\delta}$. Fig. 11 shows the artificial photosynthesis performance using different self-doped $SrTiO_{3-\delta}$ samples with gaseous CO_2/H_2O under visible light irradiations. In this process, only 2% H_2O was utilized to offer hydrogen species for CO_2 reduction because lower H_2O content may be favorable for CO_2 adsorption. Methane is the main product whose rate is enhanced from ~0.05 μmol $m^{-2}{}_{cata}$ h^{-1} for the 1200 °C sample to ~0.25 μmol $m^{-2}{}_{cata}$ h^{-1} for the 1300 °C sample under the synergetic effect of visible light

Table 3 Control experiments using the 1200 °C sample with different gas precursors under irradiation or dark

		Products				
No.	Precursors	CH_4	O_2	CO	H_2	Condition
1st	Ar	No	No	No	No	Irradiation
2nd	CO_2	No	No	No	No	Irradiation
3rd	H_2O	No	No	No	No	Irradiation
4th	$CO_2 + H_2O$	No	No	No	No	Dark
5th	$CO_2 + H_2O$	Yes	No	No	No	Irradiation

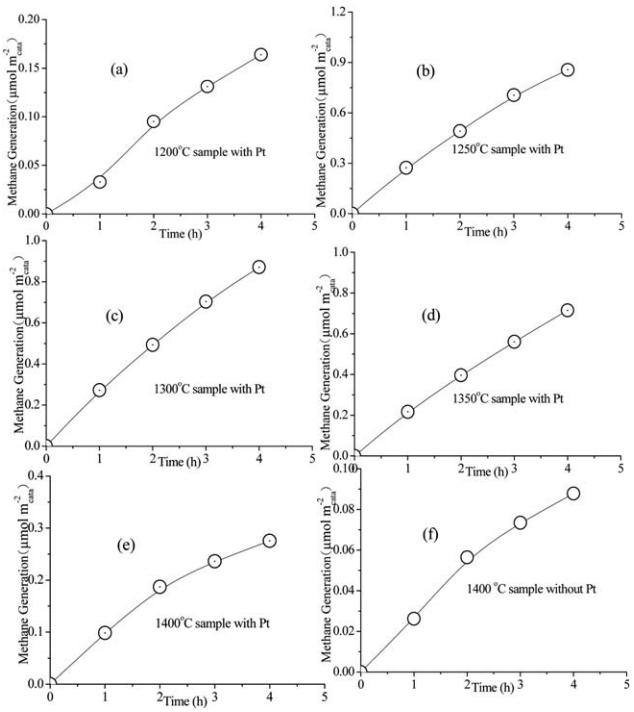

Fig. 11 Artificial photosynthesis performance with samples treated in Ar: (a) 1200, (b) 1250, (c) 1300, (d) 1350, (e) 1400, and (f) 1400 °C without Pt.

absorption and chemical adsorption of CO_2. However, the methane rate drastically decreased for 1350 and 1400 °C samples though the visible light absorption and chemical adsorption of CO_2 were continuously enhanced. At this stage, the recombination of electron and hole might be the limitations that lead to the degradation of photosynthesis. Additionally, we also conducted the experiment under irradiation with 600 nm wavelength (~2.07 eV) and confirmed that the artificial photosynthesis proceeded as well, which further proves the reasonability of calculation results of the in-gap band. The quantum efficiency at 600 nm was measured and calculated to be 0.21% for the 1300 °C sample. For comparison, the 1400 °C sample without Pt shows lower performance than that of the Pt-loaded one as shown in Fig. 11(e). In our experiment, Pt works as a co-catalyst to facilitate the separation of electron and hole. The collection of electron on Pt would enable the multi-electron reduction of CO_2. This may be the reason why Pt loaded samples show better performances. In this work, the turnover number was also calculated to evaluate the photocatalytic reactions. We estimate the turnover number in terms of Ti^{3+} ions in the sample and the photons consumed for methane generation. We consider that the outer atomic layer with a thickness of 10 Å initiates the artificial photosynthesis on the sample surface. (For the 1300 °C sample, $SrTiO_{2.83}$, ~4.8 g cm^{-3}, ~0.34 mol Ti^{3+} per mol $SrTiO_{2.83}$.) The amount of Ti^{3+} ions of 1 m^2 $SrTiO_{2.83}$ can be calculated from $N_{surf}(Ti^{3+}) = 1/5 \times m/M \times 0.34$, where m and M signify the mass and molar mass of $SrTiO_{2.83}$ on the surface. Here the $N_{surf}(Ti^{3+})$ is calculated to be 1.7 μmol for 1 m^2 $SrTiO_{2.83}$. The methane evolution under visible-light irradiation in 4 h in the reaction consumes 7.2 μmol photons. The turnover number for 4 h is therefore 7.2/1.7 = 4.2. Actually, the bulk Ti^{3+} might be also involved in reaction for the consumption of oxygen species.

It should be noted that no oxygen evolution was detected in all of the above artificial photosynthesis processes, which demonstrates that the CO_2/H_2O was not sufficiently photo-oxidized to reach the oxygen evolution though the reduced products proceed to generate accompanied by the consumption of excited electrons. The oxygen from CO_2/H_2O seems to be incorporated into the $SrTiO_{3-\delta}$ powder,[41,42] which is expected to simultaneously result in the consumption of holes as well as the oxidation of self-doped $SrTiO_{3-\delta}$ ($Ti^{3+} \rightarrow Ti^{4+}$). In order to further confirm the above speculation, we conducted an EPR test of the 1200 °C sample before and after photosynthesis experiments (7-day experiment). As shown in Fig. 12, the EPR signal at $g = 1.975$ (the characteristics of paramagnetic Ti^{3+}) of the 1200 °C sample after experiment is obviously lower than that of the sample before the experiment, confirming the decrease of Ti^{3+} content as well as the oxygen deficiency in $SrTiO_{3-\delta}$. In order to further support this evidence, we also conducted XRD tests for the 1200 °C sample before and after the experiment. The incorporation of oxygen is expected to lead to the change of cell volume of the sample. As shown in Fig. 13, a slight left shift of 2Θ was observed for the sample after irradiation for 3 days which is caused by the incorporation of oxygen into the sample leading to the increase of cell volume. It is therefore reasonable to conclude that the oxygen vacancy and high-spin Ti^{3+} not only contribute to the enhancement of visible light activity and adsorption of CO_2 but also serve as a specific sacrificial agent to achieve the

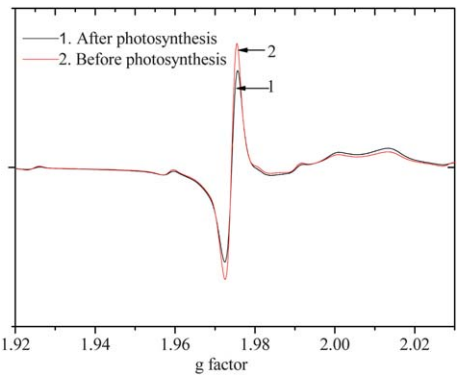

Fig. 12 EPR (120 K) of the 1200 °C sample without Pt loading before and after artificial photosynthesis.

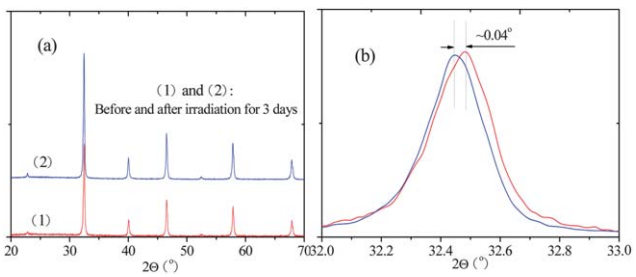

Fig. 13 XRD of the 1200 °C sample before and after artificial photosynthesis for 3 days: (a) with 2Θ ranging from 20 to 70° and (b) 2Θ ranging from 32 to 33°.

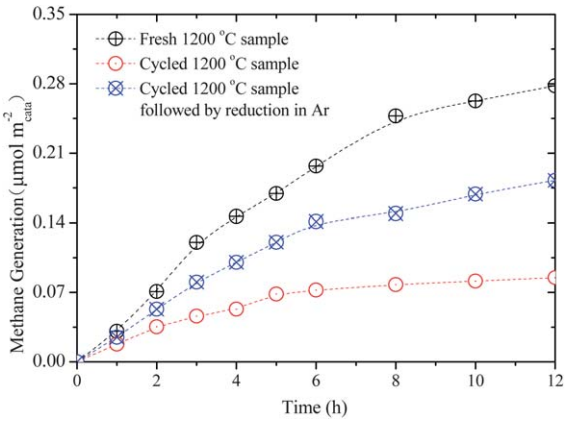

Fig. 14 Artificial photosynthesis of 1200 °C samples: (1) fresh sample; (2) cycled sample and (3) cycled sample after treatment in Ar at 1200 °C.

generation of reduced products in photosynthesis. However, the continuous consumption of Ti^{3+} in $SrTiO_{3-\delta}$ may result in the degradation of photosynthesis performance. Actually, in our experiments, the photosynthesis significantly declined in the initial 10 hours though it still proceeded even after a 3-day continuous test. But it may be possible that the performance could be recovered again by treating $SrTiO_{3-\delta}$ in Ar to introduce Ti^{3+} as well as the oxygen vacancy. As shown in Fig. 14, the cycled performance of the 1200 °C sample greatly decreased in contrast to the fresh sample, which might be attributed to the consumption of Ti^{3+}. However, reasonable recovery of artificial photosynthesis performance was also achieved by again treating the cycled sample in Ar at 1200 °C to introduce more Ti^{3+} in the sample.

Conclusions

In summary, we reported self-doped $SrTiO_{3-\delta}$ photocatalysts with enhanced visible light activity for photosynthesis from CO_2/H_2O. Experimental results and theoretical calculations together confirm that it is the oxygen vacancy and Ti^{3+} that induce an in-gap band to enhance the visible light absorption. It was demonstrated that the oxygen deficiency related defects tend to promote chemical adsorption of CO_2. The synergetic effect of light absorption and chemical adsorption of CO_2 together enhance the artificial photosynthesis under visible light. The incorporation of oxygen from CO_2/H_2O into $SrTiO_{3-\delta}$ photocatalysts leads to the absence of oxygen evolution as well as the oxidation of Ti^{3+} to Ti^{4+} in $SrTiO_{3-\delta}$. We also demonstrated the recovery of artificial photosynthesis performance by again treating the sample in Ar to introduce Ti^{3+} as well as the oxygen vacancy. Improvements of the performance could be further implemented by developing nano-size or mesoporous photocatalysts with high surface areas.

Acknowledgements

This work was in part supported by the World Premier International Research Center Initiative on Materials Nanoarchitectonics, MEXT, the JST PRESTO program and the global COE Program of Tokyo Institute of Technology, Japan.

References

1 M. I. Hoffert, K. Caldeira, G. Benford, D. R. Criswell, C. Green, H. Herzog, A. K. Jain, H. S. Kheshgi, K. S. Lackner, J. S. Lewis, H. D. Lightfoot, W. Manheimer, J. C. Mankins, M. E. Mauel, L. J. Perkins, M. E. Schlesinger, T. Volk and T. M. L. Wigley, *Science*, 2002, **298**, 981–987.
2 S. Sista, Z. Hong, L. Chen and Y. Yang, *Energy Environ. Sci.*, 2011, **4**, 1606–1620.
3 K. Xie, Y. Q. Zhang, G. Y. Meng and J. T. S. Irvine, *J. Mater. Chem.*, 2011, **21**, 195–198.
4 K. Xie, Y. Q. Zhang, G. Y. Meng and J. T. S. Irvine, *Energy Environ. Sci.*, 2011, **4**, 2218–2222.
5 K. Xie, R. Q. Yan, X. X. Xu, X. Q. Liu and G. Y. Meng, *J. Power Sources*, 2009, **187**, 403–406.
6 Z. G. Yi, J. H. Ye, N. Kikugawa, T. Kako, S. Ouyang, H. Stuart-Williams, H. Yang, J. Cao, W. Luo, Z. Li, Y. Liu and R. Withers, *Nat. Mater.*, 2010, **9**, 559–564.
7 N. Zhang, S. Ouyang, P. Li, Y. Zhang, G. Xi, T. Kako and J. H. Ye, *Chem. Commun.*, 2011, **47**, 2041–2043.
8 Q. Liu, Y. Zhou, J. Kou, X. Chen, Z. Tian, J. Gao, S. Yan and Z. Zou, *J. Am. Chem. Soc.*, 2010, **132**, 14385–14387.
9 H. Tong, N. Umezawa, J. H. Ye and T. Ohno, *Energy Environ. Sci.*, 2011, **4**, 1684.
10 H. S. Chung, C. S. H. Chen, R. A. Kremer, J. R. Boulton and G. W. Burdette, *Energy Fuels*, 1999, **13**, 641–649.
11 B. R. Eggins, P. K. J. Robertson, E. P. Murphy, E. Woods and J. T. S. Irvine, *J. Photochem. Photobiol., A*, 1998, **118**, 31–40.
12 J. T. S. Irvine, B. R. Eggins and J. Grimshaw, *Sol. Energy*, 1990, **45**, 27–33.
13 R. Carr and G. Somorjai, *Nature*, 1981, **290**, 576–577.
14 F. Wagner and G. Somorjai, *Nature*, 1980, **285**, 559–560.
15 W. Wei, Y. Dai, M. Guo, L. Yu, H. Jin, S. Han and B. Huang, *Phys. Chem. Chem. Phys.*, 2010, **12**, 7612–7619.
16 W. Wei, Y. Dai, H. Jin and B. Huang, *J. Phys. D: Appl. Phys.*, 2009, **42**, 055401.
17 H. Zhang, X. Wu, Y. Wang, X. Chen, Z. Li, T. Yu, J. Ye and Z. Zou, *J. Phys. Chem. Solids*, 2007, **68**, 280–283.
18 J. Liu, G. Chen, Z. Li and Z. Zhang, *J. Solid State Chem.*, 2006, **179**, 3704–3708.
19 D. Cuong, B. Lee, K. Choi, H. Ahn, S. Han and J. Lee, *Phys. Rev. Lett.*, 2007, **98**, 115503.
20 F. Cordero, *Phys. Rev. B: Condens. Matter Mater. Phys.*, 2007, **76**, 172106.
21 G. Bond, *Heterogeneous Catalysis—Principles and Applications*, Oxford Chemistry Series, Clarendon Press, Oxford, 2nd edn, 1987, p. 113.
22 H. Viana and J. T. S. Irvine, *Solid State Ionics*, 2002, **178**, 717–722.
23 C. Randorn and J. T. S. Irvine, *J. Mater. Chem.*, 2010, **20**, 8700–8704.
24 V. Anisimov, J. Zaanen and O. Andersen, *Phys. Rev. B: Condens. Matter*, 1991, **44**, 943–954.
25 J. Perdew and A. Zunger, *Phys. Rev. B*, 1981, **23**, 5048.
26 G. Kresse and J. Hafner, *Phys. Rev. B: Condens. Matter*, 1993, **47**, 558–561.
27 G. Kresse and J. Furthmüller, *Phys. Rev. B: Condens. Matter*, 1996, **54**, 11169–11186.
28 B. Morgan and G. Watson, *Phys. Rev. B: Condens. Matter Mater. Phys.*, 2009, **80**, 233102.
29 A. Okazaki and M. Kawaminami, *Mater. Res. Bull.*, 1973, **8**, 545.
30 A. Maegli, S. Yoon, E. Otal, L. Karvonen, P. Mandaliev and A. Weidenkaff, *J. Solid State Chem.*, 2011, **184**, 929–936.
31 M. Glinchuk, I. Bykov, A. Slipenyuk, V. Laguta and L. Jastrabik, *Phys. Solid State*, 2001, **43**, 841–844.
32 F. Zuo, L. Wang, T. Wu, Z. Zhang, D. Borchardt and P. Feng, *J. Am. Chem. Soc.*, 2010, **132**, 11856–11857.
33 C. Lin, S. Qiu, J. Chen, J. Tranqyada and M. Strongin, *Phys. C*, 1989, **162–164**, 1325–1326.
34 J. Corneille, J. He and D. Goodman, *Surf. Sci.*, 1994, **306**, 269–278.
35 J. Ruiz-Morales, J. Canales-Vazquez, C. Savaniu, D. Marrero-Lopez, W. Zhou and J. T. S. Irvine, *Nature*, 2006, **439**, 568–571.
36 H. Jina, J. Zhu, P. Ehrhart, F. Fitsilis, C. Jia, S. Regnery, K. Urbanb and R. Waserb, *Thin Solid Films*, 2003, **429**, 282–285.
37 J. Rasko and F. Solymosi, *J. Phys. Chem.*, 1994, **98**, 7147–7715.
38 B. Azambre, L. Zenboury, J. Weber and P. Burg, *Appl. Surf. Sci.*, 2010, **256**, 4570–4581.

39 J. Wang, O. Novaro, X. Bokhimi, T. Lopez, R. Gomez, J. Navarrete, M. Llanos and E. LopezSalinas, *J. Phys. Chem. B*, 1997, **101**, 7448–7451.
40 A. Cabrera, F. Vargas and R. Zarate, *J. Phys. Chem. Solids*, 1994, **55**, 1303–1307.
41 J. T. S. Irvine, D. Corcoran, A. Lashtabeg and J. Walton, *Solid State Ionics*, 2002, **154**, 447–453.
42 C. Argirusis, F. Voigts, P. Datta, J. Grosse-Brauckmanna and W. Maus-Friedrichsc, *Phys. Chem. Chem. Phys.*, 2009, **11**, 3152–3157.